# Mechanism of hard nanomaterial clearance by the liver

Kim M. Tsoi, Sonya A. MacParland, Xue-Zhong Ma, Vinzent N. Spetzler, Juan Echeverri, Ben Ouyang, Saleh M. Fadel, Edward A. Sykes, Nicolas Goldaracena, Johann M. Kaths, John B. Conneely, Benjamin A. Alman, Markus Selzner, Mario A. Ostrowski, Oyedele A. Adeyi, Anton Zilman, Ian D. McGilvray, and Warren C. W. Chan

# Mechanism of hard nanomaterial clearance by the liver

Kim M. Tsoi[a,b,*], Sonya A. MacParland[c,*], Xue-Zhong Ma[d], Vinzent N. Spetzler[d], Juan Echeverri[d], Ben Ouyang[a], Saleh M. Fadel[c], Edward A. Sykes[a], Nicolas Goldaracena[d], Johann M. Kaths[d], John B. Conneely[d], Benjamin A. Alman[e], Markus Selzner[d], Mario A. Ostrowski[c], Oyedele A. Adeyi[f], Anton Zilman[a,g], Ian D. McGilvray[d,#], Warren C.W. Chan[a,h,i,j,k,#]

[*]These authors contributed equally to this work
[#]Co-corresponding authors: warren.chan@utoronto.ca and Ian.McGilvray@uhn.ca

## Abstract

The liver and spleen are major biological barriers to translating nanomedicines because they sequester the majority of administered nanomaterials and prevent delivery to diseased tissue. Here we examined the blood clearance mechanism of administered hard nanomaterials in relation to blood flow dynamics, organ microarchitecture, and cellular phenotype. We found that nanomaterial velocity slows down 1000-fold as they enter and traverse the liver, leading to 7.5 times more nanomaterial interaction with hepatic cells relative to peripheral cells. In the liver, Kupffer cells (84.8%±6.4%), hepatic B cells (81.5±9.3%), and liver sinusoidal endothelial cells (64.6±13.7%) interacted with administered PEGylated quantum dots but splenic macrophages took up less (25.4±10.1%)

[a]Institute of Biomaterials and Biomedical Engineering, University of Toronto, Rosebrugh Building, Room 407, 164 College Street, Toronto, Ontario, Canada, M5S 3G9
[b]Division of Orthopaedic Surgery, University of Toronto, 149 College Street, Toronto, Ontario, Canada, M5T 1P5
[c]Department of Immunology, University of Toronto, Medical Sciences Building, Room 6271, 1 King's College Circle, Toronto, Ontario, Canada, M5S 1A8
[d]Multi Organ Transplant Program, Toronto General Research Institute, University Health Network, 200 Elizabeth Street, Toronto, Ontario, Canada, M5G 2C4
[e]Department of Orthopaedic Surgery, Duke University, Duke University Medical Center, Room 2888, 200 Trent Drive, Durham, North Carolina, USA, 27710
[f]Department of Pathology, Toronto General Hospital, 200 Elizabeth Street, Toronto, Ontario, Canada, M5G 2C4
[g]Department of Physics, University of Toronto, 60 St. George Street, Toronto, Ontario, Canada, M5S 1A7
[h]Terrence Donnelly Centre for Cellular and Biomolecular Research, University of Toronto, 160 College Street, Room 230, Toronto, Ontario, Canada, M5S 3E1
[i]Department of Chemical Engineering, University of Toronto, 200 College Street, Toronto, Ontario, Canada, M5S 3E5
[j]Department of Chemistry, University of Toronto, 80 St George Street, Toronto, Ontario, Canada, M5S 3H6
[k]Department of Material Science and Engineering, University of Toronto, 160 College Street, Room 450, Toronto, Ontario, Canada, M5S 3E1

due to differences in phenotype. Uptake patterns were similar for two other nanomaterial types and five different surface chemistries. Potential new strategies to overcome off-target nanomaterial accumulation may involve manipulating intra-organ flow dynamics and modulating cellular phenotype to alter hepatic cell interaction.

**Main**

Nanomaterial targeting is impeded by liver clearance

The concept of the "magic bullet" popularized by Paul Erlich describes the design of therapeutic agents that selectively attack pathogens and diseased tissue but leave healthy cells untouched. This idea has inspired the fields of nanotechnology and bioengineering, leading to huge investments in the development of agents to more efficiently diagnose and treat human diseases, such as cancer[1], diabetes[2] and atherosclerosis[3]. Researchers have produced nanoscale materials with unique optical, physical, and electrical properties that can encapsulate a drug or contrast agent and be coated with homing ligands. *In vitro* studies have shown that nanomaterials are capable of killing and/or imaging cells[4-7]. However, this success has not carried over to human use, largely due to a delivery problem. *In vivo*, the majority of the injected dose is cleared from the bloodstream by cells of the mononuclear phagocyte system (MPS) and most nanomaterials never reach their intended site[8]. The MPS is a network of immune and architectural cells, located in organs such as the liver, spleen and bone marrow, which remove foreign material from the bloodstream. Biodistribution studies have shown this to be the case for all types of nanomaterials – micelles[9,10], quantum dots[11,12], gold nanoparticles[13,14], and carbon nanotubes[15,16]. Accumulation in the MPS is the single biggest hurdle to the clinical translation of nanotechnology because it impedes delivery of a sufficient nanomaterial dose to the disease site and raises toxicity concerns. Nano-researchers often treat the MPS as a 'blackbox',

which has led to a poor understanding of the nanomaterial-MPS interaction and a lack of effective solutions.

Role of organ microarchitecture in hard nanomaterial clearance

To elucidate the mechanism of nanomaterial clearance, we first analyzed ~~nanomaterial~~ accumulation from a whole organ perspective. We used three model hard nanomaterials – quantum dots, gold nanoparticles, and silica nanoparticles as these materials can be synthesized with a narrow size distribution in the nanoscale (diameter of 1-100nm~~m size range~~) and are amenable to conjugation with a wide range of functional ligands. Consequently, they permit investigation into the impact of size, composition and surface chemistry on nanomaterial~~, allow comparison of chemical composition effects, and can be easily modified to permit exploration of the impact of surface chemistry on~~ sequestration without the added variables of deformation and degradation that are ~~(~~common for soft nanomaterials such as liposomes, micelles and polymers~~)~~. We focused on non-degradable, hard nanomaterials as their physicochemical properties are more likely to remain stable throughout the course of an *in vivo* experiment. In this manner, key design features can be evaluated and the findings can provide a foundation for future experiments that explore additional variables to ultimately define a general mechanism of liver sequestration for all hard and soft nanomaterials. ~~The non-degradable aspect of the hard nanomaterials is important as the physical-chemical parameters would likely be retained in vivo and allow us to evaluate key physical-chemical properties. This study would provide a foundation by which subsequent experiments would allow the addition of new variables in defining a general mechanism of liver sequestration for all nanomaterials.~~ In the first set of experiments, fluorescent quantum dots (see Supplementary Figure 1) were administered to Wistar rats and after four hours the liver was silver stained to visualize the nanomaterial

with bright-field microscopy. A dose of 14 μg quantum dots per gram body weight was chosen because it is comparable to recent studies[12,17] and did not result in toxicity (see Supplementary Figures 2, 3). We observed a higher amount of quantum dot accumulation in the zone surrounding the portal triad compared with the zone surrounding the central vein. Twenty-eight portal triad-central vein pairs were analyzed (see Figures 1A,B; Supplementary Figure 4) and we found both more (410 versus 42) and larger (48.5±31.5 $\mu m^2$ versus 31.2±10.8 $\mu m^2$) areas of quantum dot accumulation in the portal triad zone compared with the central vein zone (see Figures 1C, D). The same trend was found to apply to gold nanoparticles irrespective of surface chemistry; preferential peri-portal accumulation was observed for nanoparticles coated with poly(ethylene glycol) or with the cancer-targeting ligand transferrin (see Supplementary Figures 5, 6, 7, 8). Interestingly, the data also showed the importance of protein adsorption in mediating cellular sequestration (6 PEG/$nm^2$ coating versus 0.25 PEG/$nm^2$ or low versus high amounts of protein adsorption). Nanomaterial designs that experience high protein adsorption are taken up significantly more by peri-portal cells than designs with low protein adsorption (see Supplementary Figures 6,7,8; Supplementary ~~Data~~ Material 1). From these studies, two patterns emerge relating to intra-organ nanomaterial uptake. First, a cell located near the vascular inlet is more likely to take up a nanomaterial and second, this cell will accumulate more nanomaterial when compared to a cell located near the vascular outlet. In addition, the degree with ~~which hard nanomaterials are sequestered by peri-portal cells~~ which peri-portal cells sequester hard nanomaterials is related to the amount of protein adsorption. These results highlight the importance of microarchitecture in mediating nanomaterial uptake by the liver.

Role of flow dynamics in hard nanomaterial clearance

Within the liver microarchitecture, blood flow is significantly slower than in the systemic circulation. In arteries and veins, nanomaterials travel at velocities of 10-100 cm/s[18-20] but slow down to 200-800 μm/s when they enter a liver sinusoid[21,22]. We hypothesized that the reduced velocity promotes preferential nanomaterial accumulation within the sinusoid. If we assume that nanomaterials are taken up by MPS cells residing on vessel walls then heuristically, body sites with lower blood velocities will have more nanomaterial accumulation. This is because a nanomaterial will have a high chance of reaching the wall by diffusion before exiting the vessel by advection. To explore this theory, we developed a mathematical model describing the process of nanomaterial sequestration by cells. Sequestration is defined as any removal of a nanomaterial from circulation due to its interaction with a cell and includes both binding to the cell surface and internalization into the cell cytoplasm. The vessel was modeled as a cylindrical channel of length, *L*, and radius, $r_0$, with a flow velocity profile, *v(r),* and cells were assumed to reside on vessel walls (see Figure 2A). Nanomaterial sequestration was ~~initially~~ modeled using an absorbing or partially absorbing boundary condition on the channel walls. The density *c(z,r,t)* of the nanomaterial inside the channel could then be described by the following equation[23,24]:

$$\frac{\partial}{\partial t}c(r,z,t)+v(r)\frac{\partial}{\partial z}c(r,z,t)=D\frac{1}{r}\frac{\partial}{\partial r}\left(r\frac{\partial}{\partial r}c(r,z,t)\right)+\frac{\partial^2}{\partial z^2}c(r,z,t) \quad (1)$$

The two principal factors that influence nanomaterial transport within a vessel – flow along the longitudinal axis (advection) and Brownian motion along the radial axis (diffusion) are represented by the second term on the left and the first term on the right, respectively. For a spherical nanomaterial of diameter, $d_{NP}$, the diffusion coefficient is $D=\frac{k_B T}{3\ d_{NP}}$.

Equation (1) can be solved to yield the probability of nanomaterial sequestration during its passage through the channel:

$$P = \sum_{i=1}^{\infty}[1 - exp\left(-\frac{DL}{Ur_0^2}\lambda_i\right)]b_i, \quad (2)$$

where $U$ is the average flow velocity and $b_i$ and $\lambda_i$ are numerical coefficients. The sequestration probability, $P$, is a decreasing function of the dimensionless parameter $\frac{Ur_0^2}{DL}$ which measures the strength of advection relative to diffusion. Using values derived empirically and from the literature, we compared the computationally predicted probability of nanomaterial sequestration in two different locations: the liver sinusoid and the systemic circulation (see Supplementary Table 1). The liver inlet (hepatic artery, portal vein) and outlet (inferior vena cava) were selected as representative of the systemic circulation. For a Poiseuille parabolic flow profile with fully absorbing walls, the model predicts a $10^2$ to $10^3$ times greater probability of nanomaterial sequestration in a liver sinusoid than in the extra-hepatic circulation (see Figure 2B). As many types of flow occur *in vivo*, we tested the model's robustness by replacing the parabolic flow assumption with a flat flow profile. The prediction of higher nanomaterial sequestration within the sinusoid persists; however, the difference between regions is reduced (see Supplementary Figure 9). This finding extends to other types of flow as the shape of the flow profile *v(r)* in Equation (2) does not alter the expression for the sequestration probability $P$, only the numerical values of the coefficients, $b_i$ and $\lambda_i$. To validate our mathematical model and experimentally test our hypothesis, we isolated hepatic and peripheral blood mononuclear cells (PBMCs) from the quantum dot-treated rats and determined nanomaterial uptake via flow cytometry. As predicted by the model, hepatic cells took up significantly more quantum dots than did PBMCs. The trend persisted when we looked specifically at cells in the monocyte-macrophage lineage (CD68+ cells) as 67.1±15.7% of Kupffer cells and only 10.0± 6.3% of monocytes were quantum dot-positive (see Figures 2E,F; Supplementary Figure 10). The importance of flow dynamics is

reinforced by the fact that under static culture conditions, monocytes took up quantum dots with the same affinity as Kupffer cells (see Supplementary Figures 11, 12).

Nanomaterials that bind to a cell can either remain on its surface, return to the circulation or be internalized through receptor-mediated endocytosis, phagocytosis or pinocytosis[25-27]. To take nanomaterial-cell interactions into account, a parameter, $K$, was added to the model, which quantifies ~~. We defined $K$ as~~ the local sticking coefficient and~~probability as it~~ combines factors that affect nanomaterial binding to and internalization into a cell: cell density on the vessel wall, receptor density on the cell surface, internalization rate ($k_{in}$) and dissociation rate ($k_{off}$). $K$ is proportional to $k_{off}/k_{in}$ and varies from infinity for a completely reflective surface to zero for a completely absorbing ~~wall~~ one (see Figure 2C). The value of $K$ therefore depends on nanomaterial design, serum protein adsorption and cellular phenotype. The trend of preferential nanomaterial sequestration in the liver compared with the systemic circulation is magnified when incomplete absorption due nanomaterial-cell interactions is considered. For a 10nm nanomaterial and an intermediate $K$ of 4, the probability of sequestration in the sinusoid is ~~400~~ $10^4$ times higher than in the hepatic artery. If complete absorption is assumed, the difference is ~~2.5 times~~50-fold less (see Figure 2D; Supplementary Figure 9).

We next investigated the contribution of blood flow dynamics to the size-dependent clearance of nanomaterials from circulation. We calculated the predicted effect of nanomaterial diameter, $d_{np}$, on the probability of nanomaterial sequestration using Equation (2). The model suggests that modifying the particle diameter between 10 and 90nm does not significantly influence the probability of sequestration compared to the impact of vessel radius or blood velocity (see Figure 2B). The probability of sequestration for a 10nm nanomaterial is 1.5 times higher than for a 90nm nanomaterial within the

sinusoid. Contrastingly, the same 10nm nanomaterial is 750 times less likely to be sequestered in the extra-hepatic circulation than in the sinusoid. However, many studies show that larger nanomaterials are preferentially cleared by the liver[28-30]. This suggests a second contribution to nanomaterial clearance: the macrophage's propensity to phagocytose larger nanomaterials. Using fluorescent gold nanoparticles (see Supplementary Figure 5), we show that both primary rat Kupffer cells and immortalized murine macrophages preferentially took up larger nanoparticles (see Supplementary Figures 13 and 14). This phenomenon, reported for multiple nanomaterial types (see Supplementary Table 2), may be attributable to the surface chemistry of the nanoparticle where there is a higher surface ligand density for larger nanomaterials. Higher ligand density permits a multivalent receptor-ligand interaction between the cell and nanomaterial and is therefore more likely to lead to uptake [31,32]. Thus, nanomaterial surface chemistry does not necessarily contribute to the probability of cellular interaction but does influence how long a nanomaterial remains bound to the cell surface and whether it is internalized. A future study that investigates the role of specific adsorbed proteins in cellular binding and phagocytosis is required to fully understand sequestration.

## Intra-hepatic distribution of PEGylated quantum dots

Our first set of studies provided an organ-level view of nanomaterial clearance. We then proceeded to analyze sub-organ biodistribution. The prevailing assumption is that Kupffer cells are responsible for nanomaterial uptake by the liver; however, we hypothesized that a variety of hepatic cell types would internalize nanomaterials due to favorable flow dynamics in this organ. We deconstructed the nanomaterial-liver interaction by characterizing the distribution of quantum dots in hepatic cells at two timepoints following systemic nanomaterial administration (see Figure 3A; Supplementary

Figures 15,16,17). Our results demonstrate that twelve hours post-injection 84.8± 6.4% of Kupffer cells, 81.5±9.3% of B cells, 64.6±13.7% of endothelial cells along with a much smaller percentage of T cells and an 'other' population (CD19-, CD31- and CD68-negative mononuclear cells), took up the quantum dots (see Figure 3B; Supplementary Figure 18). Quantum dots were not detected in hepatocytes (see Figure 3A; Supplementary Figure 16). This finding is in contrast to studies suggesting that hepatocytes accumulate certain nanomaterials[33,34], potentially via the acquisition of ApoE from serum[35]. Interestingly, there was no difference in the percentage of quantum dot-positive cells between the four- and twelve-hour timepoints. While there was a trend for higher per cell uptake of quantum dots at twelve hours, the difference was not statistically significant (see Figures 3B,C; Supplementary Figure 19). Confocal and transmission electron microscopy confirmed that quantum dots were intracellular and located in membrane-bound peri-nuclear structures (see Figures 3D,F, Supplementary Figure 20). Immunofluorescence staining was performed to further validate our flow cytometry findings (see Figure 3G). The uptake data confirms our hypothesis, although we had not anticipated the extent to which B cells internalize nanomaterials. B cells contained a comparable amount of quantum dots to Kupffer cells, a cell type known to avidly phagocytose nanomaterials[12,34,36,37] (see Figure 3B). Kupffer cells had a relative MFI of 35.4±23.0 while B cells had a relative MFI 20.1±11.6 at twelve hours post-injection (see Figure 3C). While hepatic B cells have been shown to internalize microparticles[38], their role in nanomaterial clearance has not previously been described. Endothelial and 'other' cells were more weakly positive with relative MFI values of 4.1±1.5 and 2.9±1.6, respectively (see Figure 3C). Interestingly, the distribution of quantum dot positive-cells was different than the population distribution of liver cells. Endothelial and the 'other' cells were measured to be the most abundant

(23.9±16.3% and 21.8±7.1%, respectively), followed by Kupffer cells (10.2±5.2%) and finally B cells (1.8±1.4%) (see Figure 3E; Supplementary Figure 21). We verified that quantum dot exposure did not result in cellular recruitment to the liver (see Supplementary Figure 22). Combining the parameters of relative MFI and % total liver homogenate allowed us to determine the most important liver cell types involved in nanomaterial sequestration. Kupffer cells play the largest role in removing quantum dots from circulation while endothelial cells, B cells, and the 'other' cell type contribute comparably to the process (see Figure 3H). Having identified hepatic cell types responsible for quantum dot clearance, we wondered whether our findings would extend to other hard nanomaterial designs. In order to efficiently screen a range of nanomaterials, we first established that *in vitro* nanomaterial uptake by plated primary rat hepatic cells mirrors patterns observed *in vivo*. Specifically, we show that both *in vitro* and *in vivo*, quantum dot accumulation is comparable between Kupffer cells and hepatic B cells and that both cell types take up significantly more of this nanomaterial than do T cells (see Supplementary Figures 11, 23). We then measured uptake of five different designs of gold and silica nanoparticles *in vitro*, assuming that patterns would be reflective of *in vivo* behavior. We found that as for quantum dots, multiple hepatic cell types mediated uptake of the tested nanomaterials but that their relative importance varied with nanomaterial physicochemical properties (see Supplementary Figure 24).

## Role of cellular phenotype in hard nanomaterial clearance

Finally, we asked whether flow dynamics and microarchitecture could be used to predict nanomaterial uptake in the spleen. We found that nanomaterial accumulation reflects blood velocity as almost all nanomaterials were found within the red pulp region (see Figure 4A). Washout studies have demonstrated that blood preferentially slows down

232 in the red pulp, where it has a half-life of ~10 minutes[39,40]. Like the hepatic sinusoid, the
233 red pulp is rich in macrophages (see Supplementary Figure 25). As macrophages in the
234 hepatic sinusoid and the splenic red pulp are exposed to nanomaterial-containing blood
235 flowing at a very slow rate, we hypothesized that quantum dot uptake would be comparable
236 between the two macrophage types. However, when we analyzed quantum dot uptake in
237 splenic mononuclear cells isolated from quantum dot-treated rats, we found that splenic
238 macrophages took up significantly less nanomaterial than Kupffer cells. Twelve hours
239 post-injection, only 25.4±10.1% of splenic macrophages were quantum dot-positive,
240 compared to 84.8±6.4% of Kupffer cells (see Figures 4B,C; Supplementary Figures 16, 26).
241 Splenic macrophages also took up ten times less nanomaterial on a per cell basis (see
242 Figures 4B,C). A similar trend was seen four hours post-injection (see Figure 4C;
243 Supplementary Figure 27). This suggests that cellular phenotype within the MPS also
244 contributes to uptake. Despite similar opportunity, splenic macrophages have less
245 endocytic/phagocytic affinity for nanomaterials than their counterparts in the liver. We
246 confirmed the role of cellular phenotype by comparing quantum dot uptake by primary
247 splenic and hepatic macrophages *in vitro*. As anticipated, Kupffer cells took up more
248 quantum dots than did splenic macrophages (see Figures 4D,E; Supplementary Figures 11,
249 28). At the 80nM dose, 59.9±9.0% of Kupffer cells were quantum dot-positive compared
250 with 35.1±10.4% of splenic macrophages and the MFI for Kupffer cells was approximately
251 double that for splenic macrophages. The same trend was found for other nanomaterial
252 designs (see Supplementary Figure 29). Interestingly, the liver-spleen difference is more
253 pronounced *in vivo* and this may relate to other anatomical and physiological differences
254 between the organs. First, despite their location in the 'slow flow' red pulp region of the
255 spleen, splenic macrophages may not have the same access to transiting nanomaterials as

do Kupffer cells in the liver. Second, the rat liver receives approximately 21% of the cardiac output via both the hepatic artery and the portal vein while the spleen only receives 1% via the splenic artery[18,41].

## Strategies to improve hard nanomaterial delivery

Currently, the standard practice for reducing nanomaterial accumulation in the MPS is to focus on nanomaterial design. Researchers manipulate nanomaterial dimensions and also coat the surface with anti-fouling polymers to reduce serum protein absorption[42]. Despite using a small nanomaterial shielded with poly(ethylene glycol), the most commonly used anti-fouling polymer, significant accumulation in the liver occurred demonstrating that alteration of nanomaterial physicochemical properties will not single-handedly solve the targeting problem. Our study suggests that manipulation of the host environment should be pursued as a complementary strategy. Based on our results, two potential approaches are (1) increasing the liver flow rate to decrease the probability of nanomaterial sequestration and (2) altering the phenotype of key cells to reduce their affinity for nanomaterials. We tested the feasibility of these approaches in two additional sets of experiments. First, we investigated the relationship between nanomaterial flow rate and uptake by primary rat Kupffer cells. Using standard culture techniques and a microfluidic channel system, we compared quantum dot uptake by Kupffer cells under three conditions: 'static' (0mL/min), 'fast' flow (8mL/min), and 'slow' flow (0.6mL/min) (see Figure 5A). As anticipated, increasing the flow rate reduced quantum dot uptake. Under static conditions, 48.1±8.9% of Kupffer cells were quantum dot-positive. This reduced to 16.2±2.5% quantum dot-positive cells under 'slow' flow conditions and even further to 8.4±2.9% under 'fast' flow conditions (see Figures 5B,C). These results demonstrate that modulating flow dynamics is a feasible strategy for reducing

nanomaterial clearance by phagocytic cells. We next evaluated whether Kupffer cell phenotype could be modified to reduce nanomaterial uptake. For these experiments, we opted to use human rather than rat cells to enhance the clinical relevance of our findings and isolated Kupffer cells from the resected caudate lobes of livers used for transplantation. Kupffer cells were either left untouched or stimulated with a cytokine cocktail[43] before incubation with the nanomaterial. Uptake of fluorescent gold nanoparticles was reduced by an average of 37% by immune modulation (see Figures 5D,E). We therefore suggest~~propose~~ that manipulating cellular phenotype is a viable strategy to reduce nanomaterial uptake by macrophages. Techniques to alter both hepatic sinusoidal blood velocity and macrophage phenotype *in vivo* have been reported[44,45] and consequently we believe that these two novel approaches are appropriate for in depth investigation in the future.

## Mechanism of hard nanomaterial clearance by the liver

Putting the modeling and experimental results together, we propose the following mechanism for the sequestration of hard nanomaterials by the liver (see Figure 6). First, nanomaterials circulating in the bloodstream slow down by a factor of 1000 when they enter the liver, increasing the probability for nanomaterial clearance by cells. The amount and rate of cellular uptake is dependent upon each cell's phenotype, internalization and dissociation kinetics as well as its relative position within the liver microarchitecture. Ultimately, nanomaterials are cleared primarily by Kupffer cells, endothelial cells, B cells and an 'other' cell type. Nanomaterials that do not get taken up leave the organ through the central vein, rejoin the systemic circulation and may return to the liver during a subsequent pass. In this way, our hard nanomaterials are cleared from the bloodstream over time. Future work is required to determine whether the proposed mechanism can be applied to

soft nanomaterials such as micelles and liposomes. The solution to the nanomaterial delivery problem will likely combine optimization of nanomaterial design with a pharmaceutical liver pre-conditioning strategy, as suggested by the proof-of-concept data. In order to fulfill the promise of nanomaterials for the improved diagnosis and treatment of human disease, the liver barrier must be solved. This study represents the first glimpse into the 'blackbox' and provides a foundation for future studies to improve the targeting efficiency of nanomaterials.

## Figure Captions

**Figure 1 | Distribution of quantum dots in the liver following systemic intravascular injection. A,** Silver-stained section of a rat liver that was perfused four hours post-quantum dot injection (counter-stained with hematoxylin). Shown is one repeating unit of the liver microarchitecture. Blood flows into the liver via the hepatic artery and portal vein located in the portal triad. Blood flows out of the liver via the central vein. A zone with a radial distance of 100μm was traced around each vascular unit. Scale bar, 100$\mu m$. **B**, Overview of the image processing utilized to measure quantum dot accumulation in the zones bordering the portal triad and central vein. First, the zone surrounding each vascular structure was extracted using a radius of 100 μm from the vessel border. Second, the image was converted into a binary format and thresholded to isolate reduced silver. Finally, the area of each silver stain was measured along with its (x,y) coordinates relative to the center of the vessel. The area of reduced silver corresponds to the amount of quantum dot accumulation and is represented by a color spectrum where pale blue indicates a small amount of quantum dot accumulation and dark blue indicates a large amount of quantum dot accumulation in each individual location. **C,** Twenty-eight portal triad-central vein pairs were analyzed and the results combined. Scale bar, 100$\mu m$. **D,** Scatter plot comparing the area of each region of silver staining in the zone surrounding the portal triad versus in the zone surrounding the central vein. Corresponds to the data graphically illustrated in C. Statistical significance was evaluated using a two-tailed unpaired t-test (***P<0.001). Additional portal triad-central vein pairs are included in Supplementary Figure 4.

**Figure 2 | Nanomaterial sequestration in the liver versus in the systemic circulation: mathematical modeling and *in vivo* results. A,** Model schematic (**i**). In the systemic circulation (e.g. hepatic artery, portal vein, inferior vena cava), advection due to blood flow

is the dominant factor influencing nanomaterial transport (**ii**). In the liver sinusoid, diffusion due to Brownian motion is the dominant factor influencing nanomaterial transport (**iii**). **B**, Results of the mathematical model comparing the probability of a nanomaterial being sequestered in a liver sinusoid versus in the systemic circulation. An absorbing boundary condition on the vessel wall was utilized. Impact of nanomaterial size, between 10-90nm, is demonstrated. Numerical inputs to the model are included in Supplementary Table 1. **C**, Impact of imperfect adsorption was incorporated in the local sticking ~~probability~~coefficient, *K*, where $K \mu k_{off}/k_{in}$. In the illustration, a nanomaterial reaches a cell by Brownian motion (**1**) and may bind to a cell receptor (**2**). There are then two possible scenarios. In (**3**), the nanomaterial has a higher probability of internalization into the cell cytoplasm, decreasing *K* and increasing the overall probability of sequestration. Alternatively, in (**4**), the nanomaterial has a higher probability of dissociation into the circulation, increasing K and decreasing the overall probability of sequestration. **D**, Results of the mathematical model probing the impact of varying values of *K* on the overall probability of sequestration in the systemic circulation and in the liver sinusoid for a 10nm nanomaterial. Impact of *K* on 30/60/90nm nanomaterials is included in Supplementary Figure 9. **E**, Representative flow plots comparing quantum dot uptake *in vivo* by cells in the peripheral blood (**i**, **iii**) versus in the liver (**ii**, **iv**) twelve hours post-injection. The first comparison is for all peripheral blood mononuclear cells (PBMCs, **i**) versus all cells in the total liver homogenate (**ii**). Full gating strategy is included in Supplementary Figure 10. The second comparison is for CD68+ monocytes (**iii**) with CD68+ Kupffer cells (**iv**). Shown are plots from the control vehicle-treated animal, 'Control', and the quantum dot-treated animal, 'QD Treated'. Full gating strategy for uptake in CD68+ cells is included in Supplementary Figure 16A. **F**, Percentage of quantum dot-positive cells in the peripheral

blood versus in the liver twelve hours after intravenous quantum dot injection (**i**, **iii**), where $\%QD+Cells = \%QD+Cells_{QD\ Treated} - \%QD+Cells_{Control-Treated}$. In (**i**) quantum dot uptake in all PBMCs is compared with uptake in all total liver homogenate cells. In (**iii**) quantum dot uptake in monocytes is compared with uptake in Kupffer cells. Amount of quantum dot uptake for each cell type, where *Relative Mean Fluorescence Intensity or Relative* $MFI = MFI_{QD-Treated}/MFI_{Control-Treated}$. (**ii**, **iv**). Again, in (**ii**) the comparison is made for all cells while in (**iv**) the comparison is made for CD68+ cells (monocytes versus Kupffer cells). Plotted is the mean ± s.e.m. from 8 independent replicates. Statistical significance was evaluated using a two-tailed unpaired t-test (**P<0.01, ***P<0.001).

**Figure 3 | Characterization of *in vivo* quantum dot uptake in the liver. A**, Representative flow plots illustrating quantum dot uptake in hepatic cell populations twelve hours post-injection. Shown are plots from the control vehicle-treated animal, 'Control', and the quantum dot-treated animal, 'QD Treated'. Full gating strategy is included in Supplementary Figures 15, 16 and 17. Representative flow plots for the four-hour timepoint are included in Supplementary Figure 19. **B**, Percentage of each hepatic cell type that is quantum dot-positive at the four- and twelve-hour timepoints, where $\%QD+Cells = \%QD+Cells_{QD-Treated} - \%QD+Cells_{Control-Treated}$. **C**, Amount of quantum dot uptake for each hepatic cell type at the four- and twelve-hour timepoints, where *Relative Mean Fluorescence Intensity or Relative* $MFI = MFI_{QD-Treated}/MFI_{Control-Treated}$. **D**, Confocal microscopy images demonstrating the intracellular location of quantum dots. Shown is a z-stack image of cells from the Kupffer cell-enriched fraction (**i**) and an orthogonal projection in the yz plane (**ii**). Nucleus is stained with Hoechst 33342 (blue), actin is stained with Alexa Fluor 488-labelled phalloidin (green), quantum dots appear red. Images were acquired with a 60x PlanApo oil objective (N.A 1.4) with the following excitation (ex) and emission (em) wavelengths: nuclei

($\lambda_{ex}$=405nm; $\lambda_{em}$=442/35nm), actin ($\lambda_{ex}$=473nm; $\lambda_{em}$=515/60nm), quantum dots ($\lambda_{ex}$=559nm; $\lambda_{em}$=598/45nm). Scale bars, 5$\mu m$. **E**, Relative prevalence of hepatic cell types reported as a percentage of total cells in the liver homogenate. Full gating strategy is included in Supplementary Figure 21. For **B,C** and **E**, plotted is the mean ± s.e.m. from at least 6 independent replicates for the twelve-hour timepoint and 3 independent replicates for the four-hour timepoint. Statistical significance was evaluated using a two-tailed unpaired t-test (**P<0.01, ***P<0.001, ns = not significant or P>0.05). **F**, Transmission electron microscopy images demonstrating the presence of quantum dots within peri-nuclear membrane-bound structures in a hepatic lymphocyte-like cell twelve hours post-injection. Images of a Kupffer-like cell, an endothelial-like cell are included in Supplementary Figure 20. Shown is the location of the cell within the sinusoid (**i**) where the lymphocyte plasma membrane is traced in white, the nucleus in black and the quantum dot-containing membrane-bound intracellular vesicles in yellow. For orientation, red blood cells are traced in red and hepatocytes in blue. A high-resolution image of the quantum dot-containing vesicles is included in (**ii**) where the asterisk marks corresponding structures. The inset demonstrates individual quantum dots. Scale bars in (**i**) and (**ii**), 500nm. Scale bar in inset, 100nm. **G,** Confocal images demonstrating anti-CD68 staining in quantum dot-positive and negative cells. Cells from the Kupffer cell-enriched fraction of a quantum dot-treated animal were stained with an Alexa Fluor 647-labelled anti-CD68 antibody. Shown are antibody staining only (**i**), quantum dot uptake only (**ii**) and an overlay of both channels (**iii**). The anti-CD68 antibody appears green, quantum dots appear red and co-staining is yellow. Images were acquired with a 60x PlanApo oil objective (N.A 1.4), a zoom of 1.4x with the following excitation (ex) and emission (em) wavelengths: quantum dots ($\lambda_{ex}$=559nm; $\lambda_{em}$=598/45nm), anti-CD68 ($\lambda_{ex}$=635nm; $\lambda_{em}$=705/100nm). Images were

overlayed and pseudo-color assigned in ImageJ. Scale bars, 30 $\mu m$. **H**, The relative importance of each hepatic cell type to quantum dot uptake in the liver as measured by the *Distance from Origin*, where: $Distance\ from\ Origin = \sqrt{(Relative\ MFI)^2 + (\%Total\ Liver\ Homogenate)^2}$. Hepatocytes are not represented, as quantum dot uptake was not detected.

**Figure 4 | Quantum dot uptake in the liver versus in the spleen: *in vivo* and *in vitro* results.** **A**, Quantum dot uptake in the spleen occurs primarily in the red pulp. Quantum dots are identified via silver staining (hematoxylin counter-stain). Scale bar, 100$\mu m$. **B**, Representative flow plots demonstrating the difference in quantum dot uptake between Kupffer cells and splenic macrophages twelve hours post-quantum dot injection (**i**). Corresponding histograms showing the *Mean Fluorescence Intensity (MFI)* are included in (**ii**). Shown are plots from the control vehicle-treated animal, 'Control', and the quantum dot-treated animal, 'QD Treated'. Full gating strategy is included in Supplementary Figure 16. Representative flow plots from the four-hour timepoint are included in Supplementary Figure 27. **C**, Percentage of quantum dot-positive Kupffer cells and splenic macrophages four- and twelve-hours post-quantum dot injection (**i**), where $\%QD{+}Cells = \%QD{+}Cells_{QD\text{-}Treated} - \%QD{+}Cells_{Control\text{-}Treated}$. The amount of quantum dots taken up by both cell types is shown in (**ii**), where *Relative Mean Fluorescence Intensity or Relative MFI*=$MFI_{QD\text{-}Treated}/MFI_{Control\text{-}Treated}$. Plotted is the mean ± s.e.m. from at least 6 independent replicates for the twelve-hour timepoint and 3 independent replicates for the four-hour timepoint. Statistical significance was evaluated using a two-way ANOVA with a Bonferroni post-test (**P<0.01, ***P<0.001, ns = not significant or P>0.05). **D**, Representative flow plots identifying quantum dot-positive Kupffer cells and splenic macrophages. Isolated cells were either left untreated or incubated with 40/80/160nM quantum dots. Four incubation

times were investigated; shown is the six-hour timepoint. Full gating strategy is included in Supplementary Figure 11 (**i**). Representative histograms showing the *Mean Fluorescence Intensity (MFI)* in the QD channel at baseline and after a six-hour incubation with 80nM quantum dots are included in (**ii**). **E**, Percentage of quantum dot-positive cells (**i**) and amount of quantum dot uptake (*MFI*, **ii**) for each cell type six hours post-incubation with 40nM/80nM/160nM quantum dots. $\%QD+Cells = \%QD+Cells_{QD\text{-}Treated} - \%QD+Cells_{Untreated}$ . Full time-course is included in Supplementary Figure 28. Plotted is the mean ± s.e.m. from 3 independent replicates. Statistical significance was evaluated using a two-way ANOVA with a Bonferroni post-test for the complete time-course (*P<0.05, ns = not significant or P>0.05).

**Figure 5 | Nanomaterial uptake by Kupffer cells can be reduced by manipulating flow rate and cellular phenotype.** Quantum dot uptake by primary rat Kupffer cells was compared under three conditions, traditional cell culture in a Petri dish ('static') or in a microfluidic chip with two different flow rates, 'fast' flow at 8mL/min and 'slow' flow at 0.6mL/min. **A**, Flow cytometry plots demonstrating the gating strategy (**i**) and representative plots showing differences in uptake between 'static', 'fast' and 'slow' flow conditions (**ii**). **B**, Percentage of quantum dot-positive, Annexin-negative (i.e. live) Kupffer cells under the three conditions (**i**). Amount of quantum dots taken up by Kupffer cells in each condition where, $\%QD+Cells = \%QD+Cells_{QD\text{-}Treated} - \%QD+Cells_{Untreated}$ and *Relative Mean Fluorescence Intensity or Relative* $MFI = MFI_{QD\text{-}Treated}/MFI_{Untreated}$ (**ii**). Plotted is the mean ± s.e.m. from 3 independent replicates. Statistical significance was evaluated using a two-tailed unpaired t-test (*P<0.05, **P<0.01, ns = not significant or P>0.05). **C**, Time-lapse images comparing uptake under 'slow' and 'fast' flow conditions. Quantum dots are shown in red and are marked with a white arrow in the last frame. Images were acquired with a

10X DIC Fluar objective (N.A. 0.5) with the following excitation (ex) and emission (em) wavelengths for the quantum dots: $\lambda_{ex}$=470nm; $\lambda_{em}$=605/70nm. Videos for quantum dots uptake under 'slow' and 'fast' flow conditions are included in Supplementary Videos 1,2. **D**, Primary human Kupffer cells were either left untouched, 'Freshly Isolated', or stimulated using a cytokine cocktail, 'Stimulated'. Cells were then incubated with fluorescent gold nanoparticles for four hours. Representative flow plots (**i**) and histograms (**ii**) showing the reduction in nanomaterial uptake following stimulation. **E**, Amount of nanomaterial uptake by freshly isolated versus stimulated human Kupffer cells, where *Relative Mean Fluorescence Intensity or Relative MFI=*$MFI_{AuNP\ Treated}/MFI_{Untreated}$. Plotted are the values for cells taken from four separate patients. Statistical significance was evaluated using a two-tailed paired t-test (*P<0.05).

**Figure 6 | Mechanism of nanomaterial transport in the liver.** Nanomaterials injected into the bloodstream encounter the mononuclear phagocyte system (MPS), a group of organs that contain phagocytic cells. The intensity of the blue color in the figure reflects the degree of nanomaterial uptake within each MPS organ[12] (see outline of human body, left). As the nanomaterials transition from the peripheral circulation to the liver, their velocity reduces 1000-fold. This allows the nanomaterials to interact with a variety of cells, resulting in their gradual clearance from the bloodstream. There is a concentration gradient of nanomaterials along the length of the sinusoid and the amount leaving the liver through the central vein is lower than the amount that enters via the portal triad (see image of liver lobule, bottom right). B and T cells border the portal triad and are exposed to a high concentration of incoming nanomaterials (see schematic of a liver sinusoid, top right). The difference in nanomaterial uptake between these cell types is due to the increased endocytic/phagocytic capacity of B cells compared with T cells. Nanomaterials that escape

the first set of cellular interactions move along the sinusoid and can come into contact with endothelial and Kupffer cells. Hepatocytes are separated from the bloodstream by a layer of fenestrated endothelial cells and do not take up nanomaterials. Nanomaterials that escape uptake during a pass through the liver return to the systemic circulation via the central vein and are ultimately carried back to the liver (or another MPS organ). This process repeats itself until nanomaterial clearance from the bloodstream is complete.

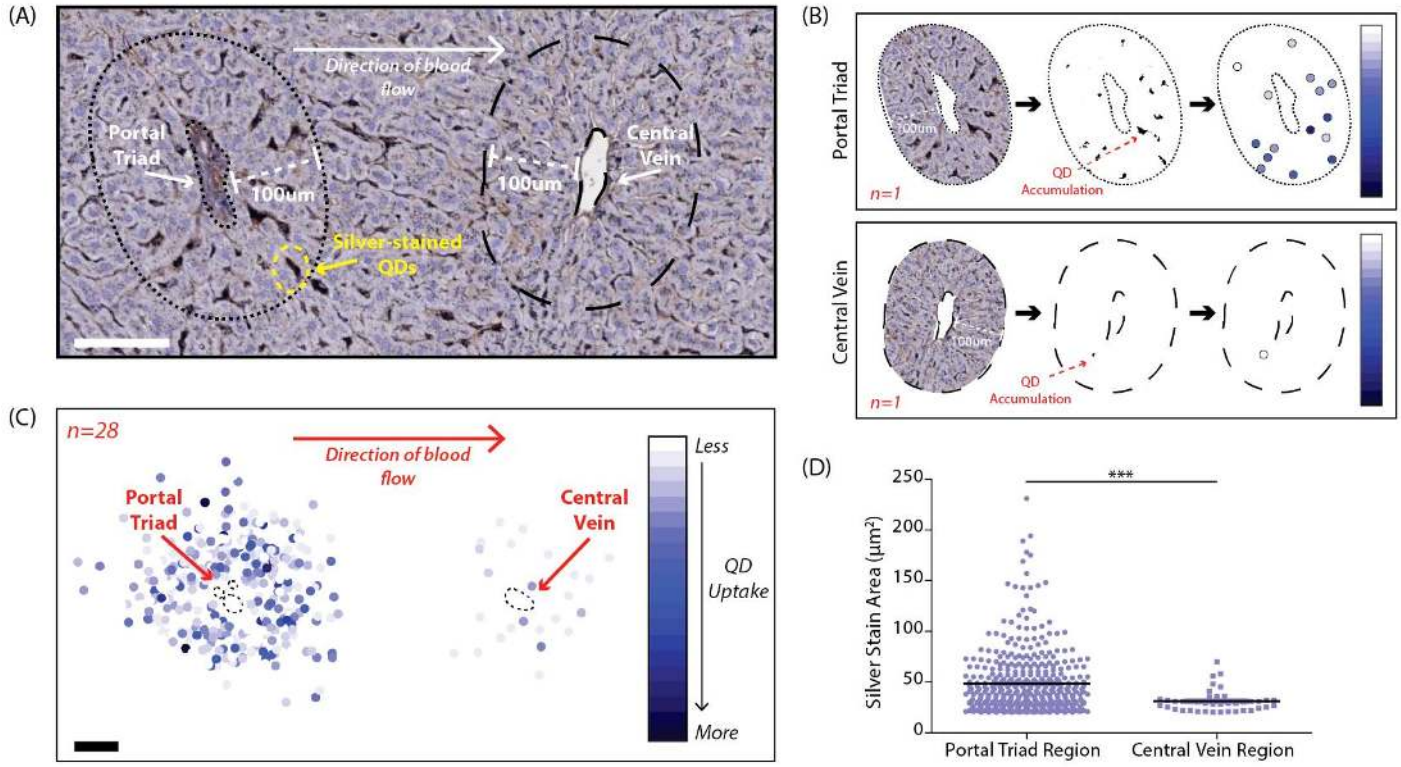


**Figure 1 | Distribution of quantum dots in the liver following systemic intravascular injection.**

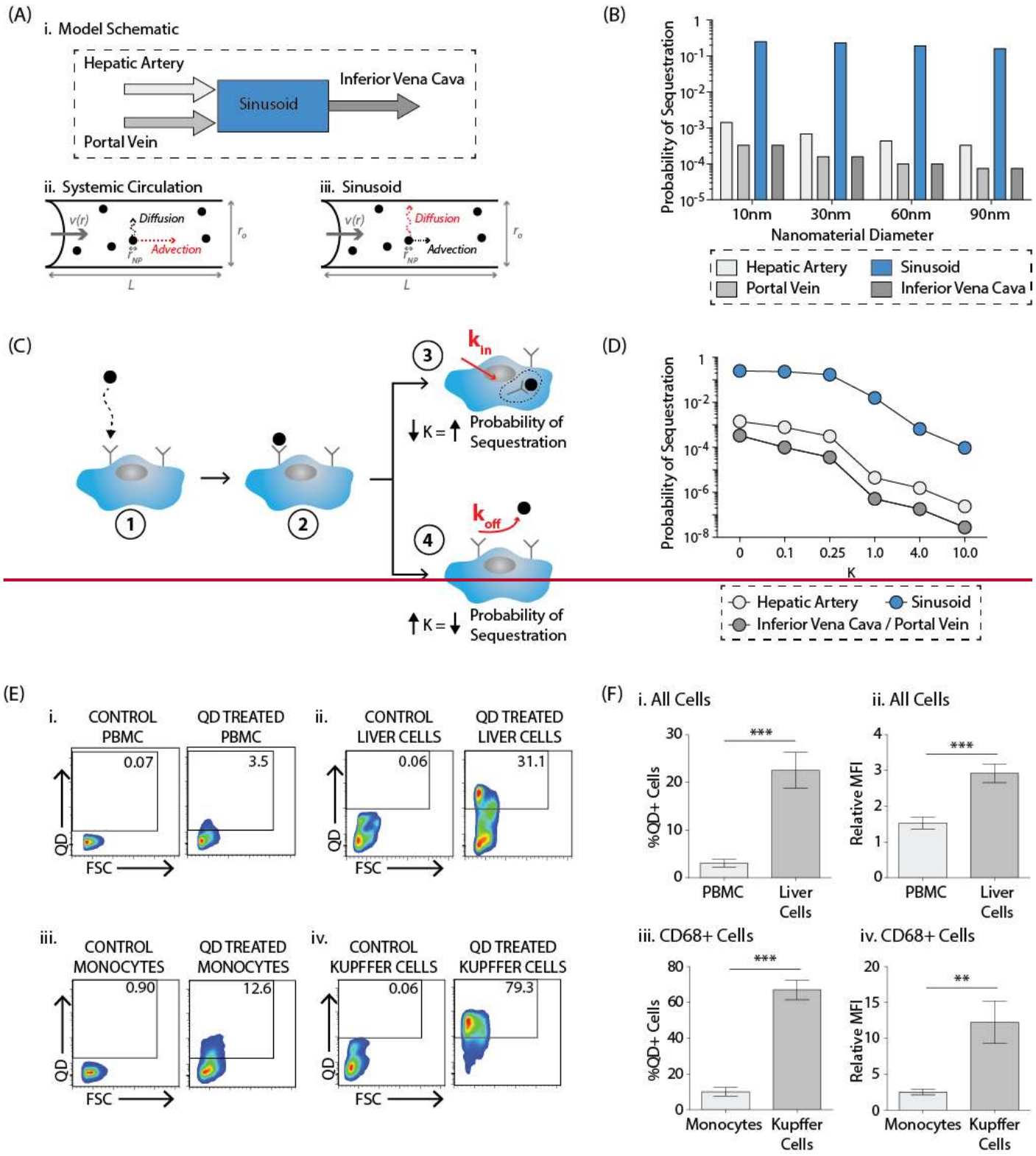
(A)
i. Model Schematic
Hepatic Artery
Inferior Vena Cava
Sinusoid
Portal Vein
ii. Systemic Circulation
iii. Sinusoid
v(r)
Diffusion
Advection
$r_o$
L
(B)
Probability of Sequestration
10nm
30nm
60nm
90nm
Nanomaterial Diameter
Hepatic Artery
Portal Vein
Sinusoid
Inferior Vena Cava
(C)
$k_{in}$
$k_{off}$
↓K = ↑ Probability of Sequestration
↑K = ↓ Probability of Sequestration
(D)
Probability of Sequestration
K
Hepatic Artery
Sinusoid
Inferior Vena Cava / Portal Vein
(E)
i. CONTROL PBMC
QD TREATED PBMC
0.07
3.5
ii. CONTROL LIVER CELLS
QD TREATED LIVER CELLS
0.06
31.1
iii. CONTROL MONOCYTES
QD TREATED MONOCYTES
0.90
12.6
iv. CONTROL KUPFFER CELLS
QD TREATED KUPFFER CELLS
0.06
79.3
QD
FSC
(F)
i. All Cells
ii. All Cells
%QD+ Cells
Relative MFI
PBMC
Liver Cells
iii. CD68+ Cells
iv. CD68+ Cells
Monocytes
Kupffer Cells

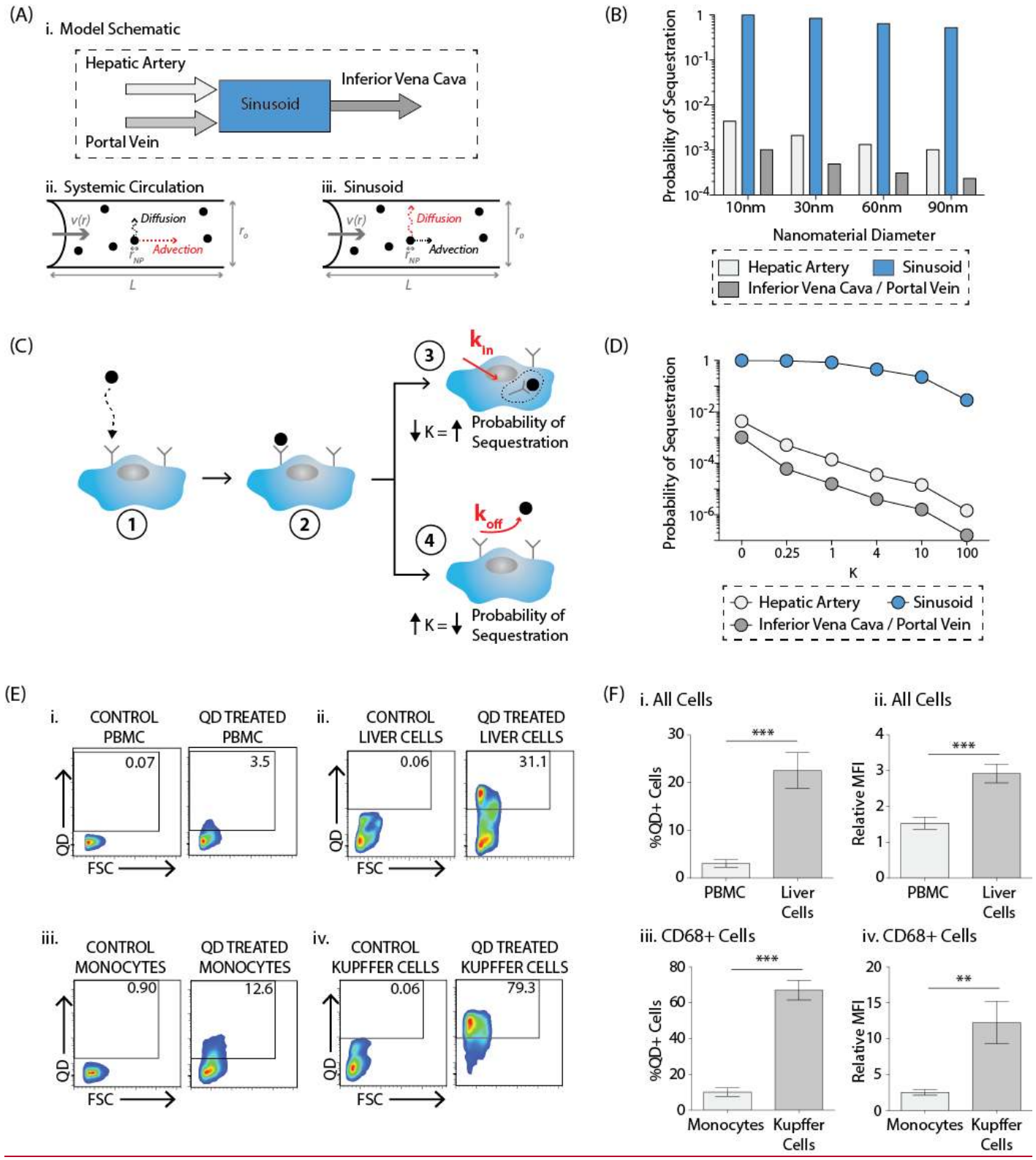


**Figure 2 | Nanomaterial sequestration in the liver versus in the systemic circulation: mathematical modeling and *in vivo* results.**

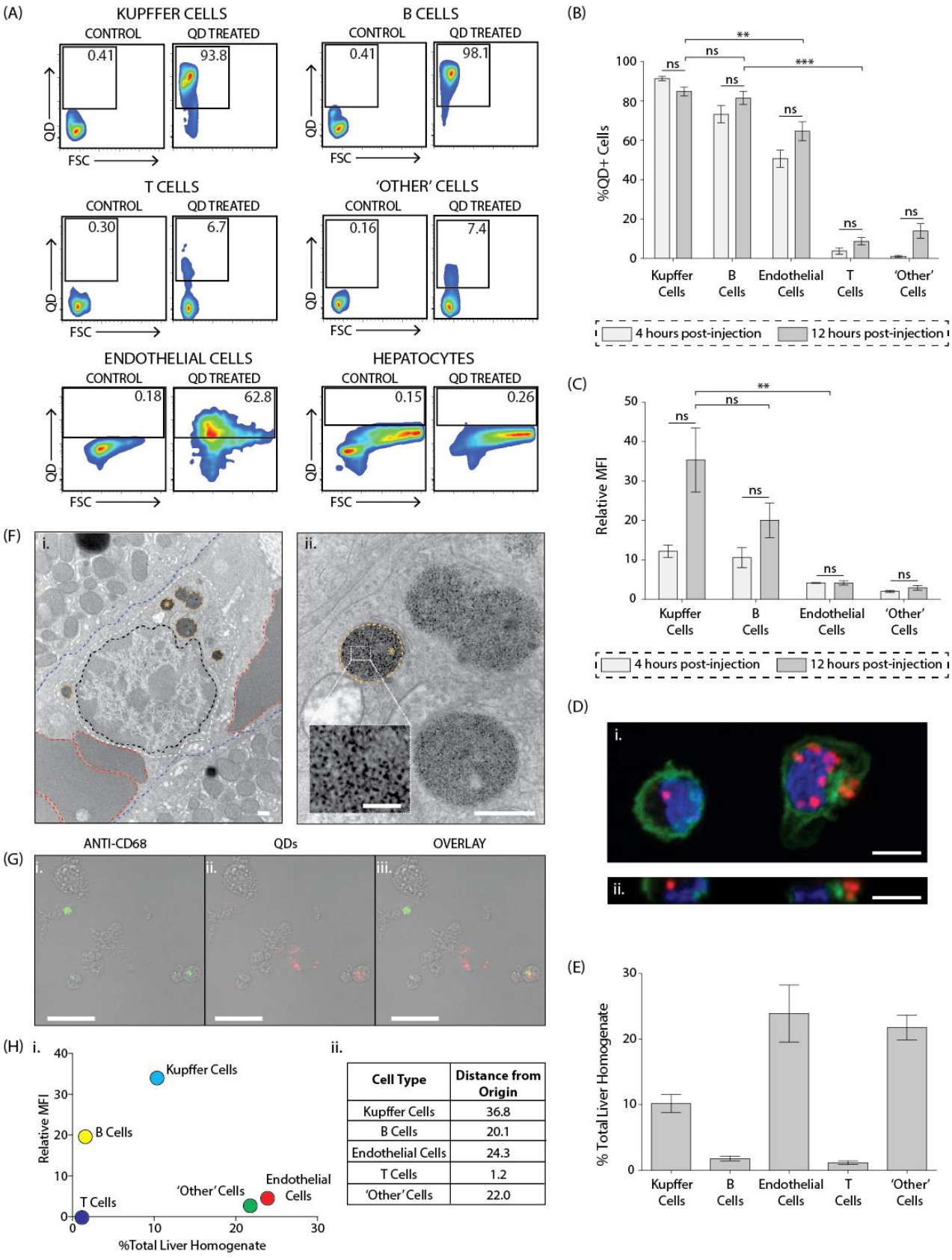


**Figure 3 | Characterization of *in vivo* quantum dot uptake in the liver.**

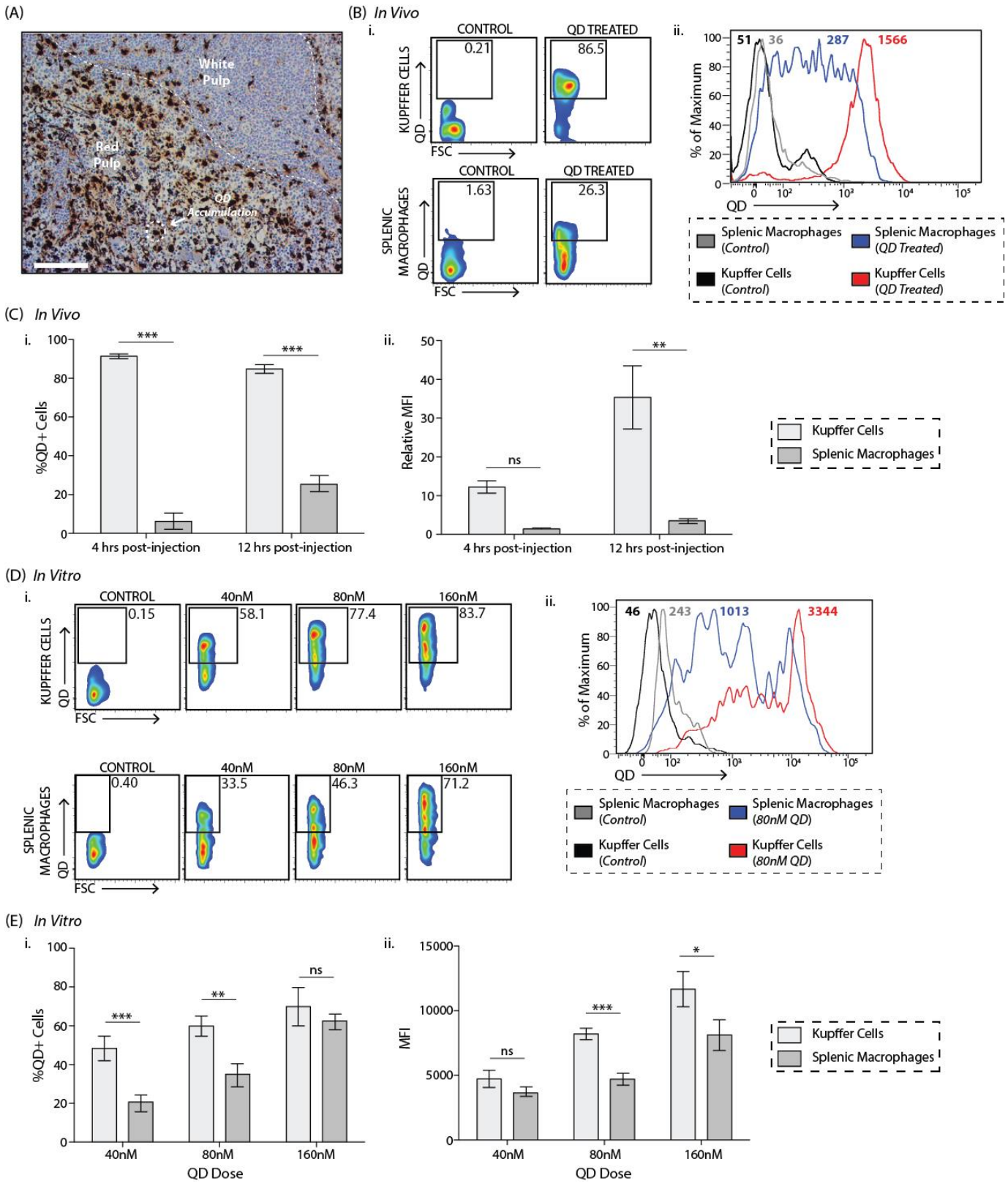


**Figure 4 | Quantum dot uptake in the liver versus in the spleen: *in vivo* and *in vitro* results.**

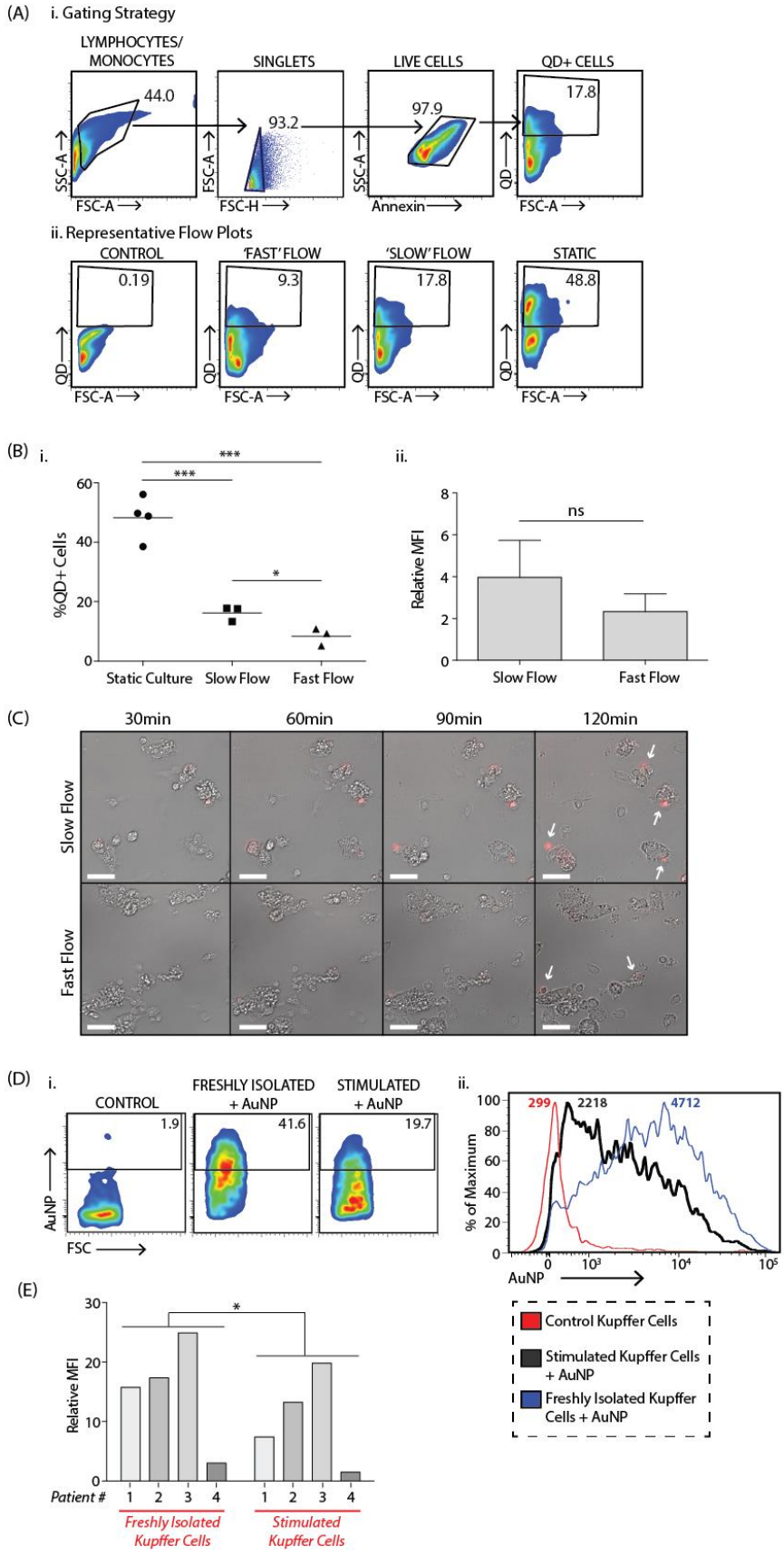


**Figure 5 | Nanomaterial uptake by Kupffer cells can be reduced by manipulating flow rate and cellular phenotype**

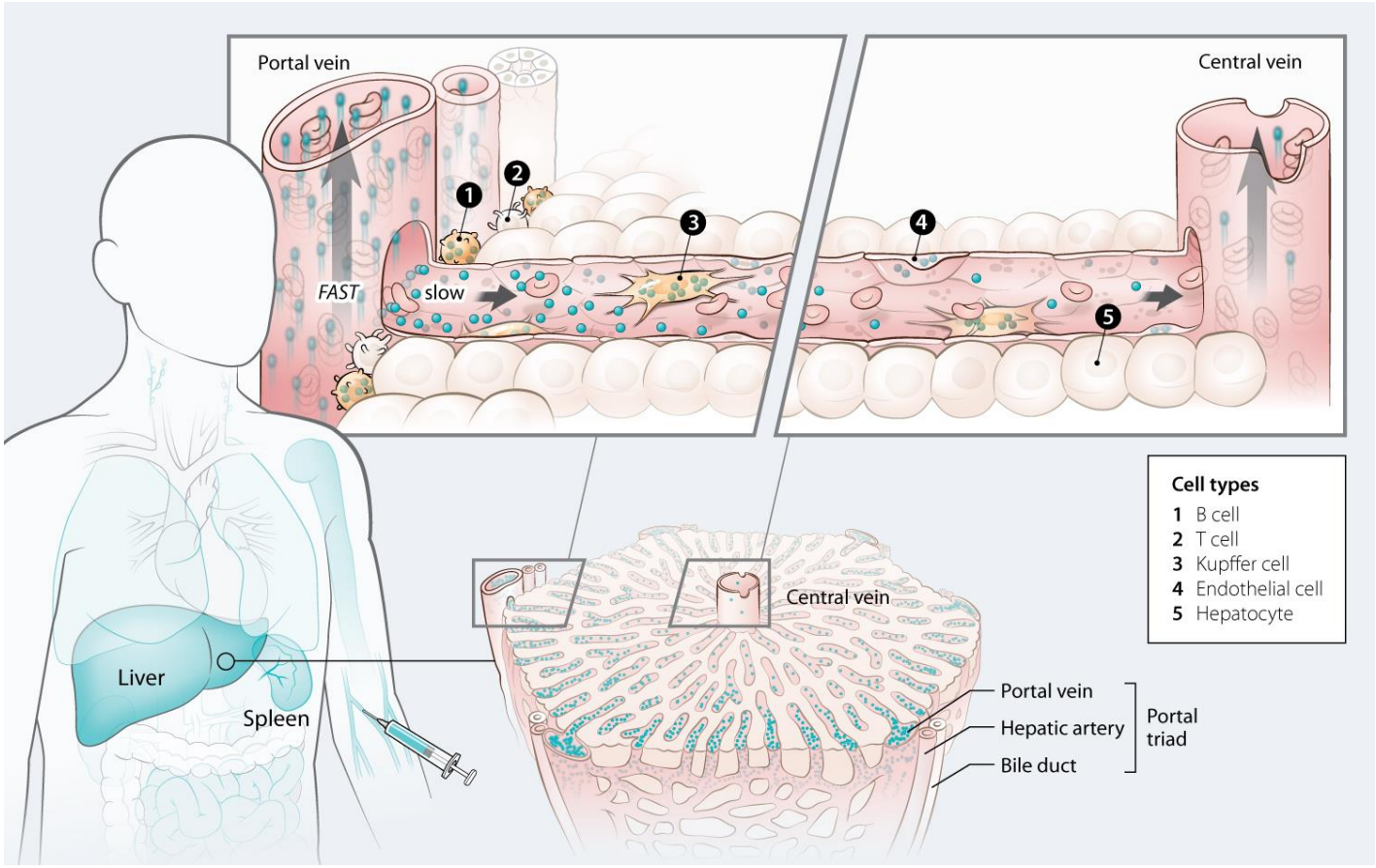


**Figure 6 | Mechanism of nanomaterial transport in the liver.**

436

## References


1. Kim, B. Y., Rutka, J. T. & Chan, W. C. Nanomedicine. *New Engl J Med* **363,** 2434–2443 (2010).
2. Veiseh, O., Tang, B. C., Whitehead, K. A., Anderson, D. G. & Langer, R. Managing diabetes with nanomedicine: challenges and opportunities. *Nat Rev Drug Discov* **14,** 45–57 (2014).
3. Mulder, W. J. M., Jaffer, F. A., Fayad, Z. A. & Nahrendorf, M. Imaging and nanomedicine in inflammatory atherosclerosis. *Sci Transl Med* **6,** 239sr1–239sr1 (2014).
4. Nasongkla, N. *et al.* Multifunctional polymeric micelles as cancer-targeted, MRI-ultrasensitive drug delivery systems. *Nano Lett* **6,** 2427–2430 (2006).
5. Jaiswal, J. K., Mattoussi, H., Mauro, J. M. & Simon, S. M. Long-term multiple color imaging of live cells using quantum dot bioconjugates. *Nat Biotechnol* **21,** 47–51 (2002).
6. Dhar, S., Daniel, W. L., Giljohann, D. A., Mirkin, C. A. & Lippard, S. J. Polyvalent oligonucleotide gold nanoparticle conjugates as delivery vehicles for platinum(IV) warheads. *J Am Chem Soc* **131,** 14652–14653 (2009).
7. Kam, N. W. S., O'Connell, M., Wisdom, J. A. & Dai, H. Carbon nanotubes as multifunctional biological transporters and near-infrared agents for selective cancer cell destruction. *P Natl Acad Sci USA* **102,** 11600–11605 (2005).
8. Wilhelm, S., Tavares, A. J., Dai, Q., Ohta, S. & Audet, J. Analysis of nanoparticle delivery to tumours. *Nat Rev Mater* **1**, 16014 (2016).
9. Zhang, C. *et al.* Pharmacokinetics, biodistribution, efficacy and safety of N-octyl-O-sulfate chitosan micelles loaded with paclitaxel. *Biomaterials* **29,** 1233–1241 (2008).
10. Fonge, H., Huang, H., Scollard, D., Reilly, R. M. & Allen, C. Influence of formulation variables on the biodistribution of multifunctional block copolymer micelles. *J Control Release* **157,** 366–374 (2012).
11. Ye, L. *et al.* A pilot study in non-human primates shows no adverse response to intravenous injection of quantum dots. *Nat Nanotechnol* **7,** 453–458 (2012).
12. Fischer, H. C., Liu, L., Pang, K. S. & Chan, W. C. W. Pharmacokinetics of nanoscale quantum dots: in vivo distribution, sequestration, and clearance in the rat. *Adv Funct Mater* **16,** 1299–1305 (2006).
13. Semmler-Behnke, M. *et al.* Biodistribution of 1.4- and 18-nm gold particles in rats. *Small* **4,** 2108–2111 (2008).
14. De Jong, W. H. *et al.* Particle size-dependent organ distribution of gold nanoparticles after intravenous administration. *Biomaterials* **29,** 1912–1919 (2008).
15. Liu, Z. *et al.* In vivo biodistribution and highly efficient tumour targeting of carbon nanotubes in mice. *Nat Nanotechnol* **2,** 47–52 (2006).
16. Yang, S. T. *et al.* Biodistribution of pristine single-walled carbon nanotubes in vivo. *J Phys Chem C* **111,** 17761–17764 (2007).
17. Hauck, T. S., Anderson, R. E., Fischer, H. C., Newbigging, S. & Chan, W. C. W. In vivo quantum-dot toxicity assessment. *Small* **6,** 138–144 (2010).
18. Kuwahira, I., Gonzalez, N. C., Heisler, N. & Piiper, J. Changes in regional blood flow distribution and oxygen supply during hypoxia in conscious rats. *J Appl Physiol* **74,** 211–214 (1993).
19. Fournier, L. S. *et al.* Early modifications of hepatic perfusion measured by functional CT in a rat model of hepatocellular carcinoma using a blood pool contrast agent. *Eur*

*Radiol* **14,** 2125–2133 (2004).
20. Miyazaki, S. *et al.* Investigation on the optimal position for the quantification of hepatic perfusion by use of dynamic contrast-enhanced computed tomography in rats. *Radiol Phys Technol* **2,** 183–188 (2009).
21. Menger, M. D., Marzi, I. & Messmer, K. In vivo fluorescence microscopy for quantitative analysis of the hepatic microcirculation in hamsters and rats. *Eur Surg Res* **23,** 158–169 (1991).
22. MacPhee, P. J., Schmidt, E. E. & Groom, A. C. Intermittence of blood flow in liver sinusoids, studied by high-resolution in vivo microscopy. *Am J Physiol-Gastr L* **269,** G692–G698 (1995).
23. Ingham, D. B. Diffusion of aerosols from a stream flowing through a cylindrical tube. *J Aerosol Sci* **6,** 125–132 (1975).
24. Davies, C. N. Diffusion and sedimentation of aerosol particles from Poiseuille flow in pipes. *J Aerosol Sci* **4,** 317–328 (1973).
25. Dobrovolskaia, M. A. & McNeil, S. E. Immunological properties of engineered nanomaterials. *Nat Nanotechnol* **2,** 469–478 (2007).
26. Lunov, O. *et al.* Differential uptake of functionalized polystyrene nanoparticles by human macrophages and a monocytic cell line. *ACS Nano* **5,** 1657–1669 (2011).
27. Wang, H., Wu, L. & Reinhard, B. M. Scavenger receptor mediated endocytosis of silver nanoparticles into J774A.1 macrophages is heterogeneous. *ACS Nano* **6,** 7122–7132 (2012).
28. Sykes, E. A., Chen, J., Zheng, G. & Chan, W. C. W. Investigating the impact of nanoparticle size on active and passive tumor targeting efficiency. *ACS Nano* **8,** 5696–5706 (2014).
29. Perrault, S. D., Walkey, C., Jennings, T., Fischer, H. C. & Chan, W. C. W. Mediating tumor targeting efficiency of nanoparticles through design. *Nano Lett* **9,** 1909–1915 (2009).
30. Cho, W.-S. *et al.* Size-dependent tissue kinetics of PEG-coated gold nanoparticles. *Toxicol Appl Pharm* **245,** 116–123 (2010).
31. Chithrani, B. D. & Chan, W. C. W. Elucidating the mechanism of cellular uptake and removal of protein-coated gold nanoparticles of different sizes and shapes. *Nano Lett* **7,** 1542–1550 (2007).
32. Gao, H. J., Shi, W. D. & Freund, L. B. Mechanics of receptor-mediated endocytosis. *P Natl Acad Sci USA* **102,** 9469–9474 (2005).
33. Cormode, D. P. *et al.* A versatile and tunable coating strategy allows control of nanocrystal delivery to cell types in the liver. *Bioconjugate Chem* **22,** 353–361 (2011).
34. Cheng, S.-H. *et al.* Visualizing dynamics of sub-hepatic distribution of nanoparticles using intravital multiphoton fluorescence microscopy. *ACS Nano* **6,** 4122–4131 (2012).
35. Akinc, A. *et al.* Targeted delivery of RNAi therapeutics with endogenous and exogenous ligand-based mechanisms. *Mol Ther* **18**, 1357-1364 (2010).
36. Sadauskas, E. *et al.* Kupffer cells are central in the removal of nanoparticles from the organism. *Part Fibre Toxicol* **4,** 10 (2007).
37. Bartneck, M. *et al.* Peptide-functionalized gold nanorods increase liver injury in hepatitis. *ACS Nano* **6,** 8767–8777 (2012).
38. Nakashima, M. *et al.* Pivotal Advance: Characterization of mouse liver phagocytic B cells in innate immunity. *J Leukocyte Biol* **91,** 537–546 (2012).
39. Stock, R. J., Cilento, E. V., Reilly, F. D. & McCuskey, R. S. A compartmental analysis of

the splenic circulation in rat. *Am J Physiol-Heart C* **245,** H17–H21 (1983).
40. Chadburn, A. The spleen: anatomy and anatomical function. *Semin Hematol* **37,** 13–21 (2000).
41. Delp, M. D., Evans, M. V. & Duan, C. Effects of aging on cardiac output, regional blood flow, and body composition in Fischer-344 rats. *J Appl Physiol* **85,** 1813–1822 (1998).
42. Walkey, C. D., Olsen, J. B., Guo, H., Emili, A. & Chan, W. C. W. Nanoparticle size and surface chemistry determine serum protein adsorption and macrophage uptake. *J Am Chem Soc* **134,** 2139–2147 (2012).
43. Jones, S. W. *et al.* Nanoparticle clearance is governed by Th1/Th2 immunity and strain background. *J Clin Invest* **123,** 3061–3073 (2013).
44. Koo, A., Liang, I. Y. & Cheng, K. K. Hepatic sinusoidal responses to intraportal injections of phenylephrine and isoprenaline in the rat. *Clin Exp Pharmacol P* **3,** 391–395 (1976).
45. Hagemann, T. *et al.* 'Re-educating' tumor-associated macrophages by targeting NF- B. *J Exp Med* **205,** 1261–1268 (2008).

**Acknowledgements**

We would to acknowledge the Canadian Institute of Health Research and Natural Sciences and Engineering Research Council for funding the project. K.M.T. thanks the NSERC Vanier Canada Graduate Scholarship Program and the Surgeon-Scientist Program at the University of Toronto for financial support. S.A.M. thanks the CASL/CIHR Hepatology Fellowship Program and the National CIHR Research Training Program in Hepatitis C for financial support. We would also like to acknowledge Melanie Peralta and Carmelita Hoculada from the University Health Network Pathology Research Program (Toronto, Canada), Doug Holmyard from the Mount Sinai Advanced Bioimaging Centre (Toronto, Canada), Feng Xu from the University Health Network Advanced Optical Microscopy Facility (Toronto, Canada), Dionne White from the Department of Immunology, University of Toronto (Toronto, Ontario), Justin Manual, Jordan Feld and Vera Cherepanov from the Toronto Centre for Liver Disease (Toronto, Canada), Jonathan Krieger from the SPARC Biocentre at the Hospital for Sick Children (Toronto, Canada) and Alexander Black from the Department of Anatomy, National University of Ireland, Galway (Galway, Ireland) for their assistance.

**Author Contributions**

KMT, SAM, JBC, IDM, WCWC conceived the idea. KMT, SAM, OAA, IDM, WCWC analyzed the data. KMT and SAM conducted the experiments with assistance from XZM, VNS, JE, BO, SMF, EAS, NG, and JMK. AZ performed the mathematical modeling. BAA, MS, MAO supervised the work.